Geophysical Research Letters

RESEARCH LETTER
10.1029/2025GL114976

Ionospheric Lamb Waves With Conical Phase Fronts Following the 2022 Tonga Eruption Unveiled by BeiDou GEO Observations

Ruoxi Li[1,2], Jiuhou Lei[1,2], Fuqing Huang[1], Feifan Liu[1], Shun-Rong Zhang[3], Xuetao Chen[1], Xiaoli Luan[1], Ziyi Yang[1], Tong Dang[1], and Xiankang Dou[2]

[1]Deep Space Exploration Laboratory/School of Earth and Space Sciences, University of Science and Technology of China, Hefei, China, [2]CAS Center for Excellence in Comparative Planetology/CAS Key Laboratory of Geospace Environment/Mengcheng National Geophysical Observatory, University of Science and Technology of China, Hefei, China, [3]Haystack Observatory, Massachusetts Institute of Technology, Westford, MA, USA

Abstract Prior observational uncertainties have hindered the clear understanding of the link between tropospheric Lamb waves and ionospheric disturbances. In this study, we precisely extracted ionospheric Lamb waves originating from the epicenter of the 15 January 2022 Tonga eruption, propagating upward in a conical structure. This was achieved by using line-of-sight observations from the BeiDou geostationary satellites, which eliminated the spatiotemporal ambiguity introduced by the relative motion of Global Positioning System satellites, enabling the clear extraction of the Lamb signal in the ionosphere. The observed L0 mode speed (~323 m/s) and period (~30 min) were consistent with those of the tropospheric Lamb wave. It suggested that the ionospheric Lamb wave is likely driven by the surface Lamb wave, leading to a conical wave-front that extends in altitude. This study highlights the significant role of Lamb waves in transmitting energy from epicenters through Earth's atmosphere and plasma systems.

Plain Language Summary Significant explosive events, such as extreme volcanic eruptions, earthquakes, meteoroid impacts, and large artificial explosions, can trigger atmospheric Lamb waves, which can travel long distances, even circling the Earth several times. While Lamb waves are generally believed to be confined to the Earth's surface, our analysis of the Lamb waves from the 2022 Tonga eruption reveals that they can also propagate in a tilted manner upward into the ionosphere. These waves manifest as a three-dimensional conical structure, expanding outward from the epicenter, with larger radii at higher altitudes and smaller ones at lower altitudes.

Key Points:

- Ionospheric Lamb waves following the 2022 Tonga eruption were precisely extracted using line-of-sight observations from Geostationary Orbit satellites
- The L0 mode exhibited upward-tilted propagation, forming a conical structure with a horizontal speed of 323 m/s in the ionosphere
- The observed ionospheric Lamb wave is likely driven by the surface Lamb as a moving source rather than re-excited in the upper atmosphere

Supporting Information:

Supporting Information may be found in the online version of this article.

Correspondence to:

J. Lei,
leijh@ustc.edu.cn

Citation:

Li, R., Lei, J., Huang, F., Liu, F., Zhang, S.-R., Chen, X., et al. (2025). Ionospheric Lamb waves with conical phase fronts following the 2022 Tonga eruption unveiled by BeiDou GEO observations. *Geophysical Research Letters*, *52*, e2025GL114976. https://doi.org/10.1029/2025GL114976

Received 24 JAN 2025
Accepted 30 APR 2025

Author Contributions:

Funding acquisition: Jiuhou Lei
Methodology: Ruoxi Li
Software: Fuqing Huang
Supervision: Jiuhou Lei
Writing – original draft: Ruoxi Li
Writing – review & editing: Jiuhou Lei, Fuqing Huang, Feifan Liu, Shun-Rong Zhang, Xuetao Chen, Xiaoli Luan, Ziyi Yang, Tong Dang, Xiankang Dou

1. Introduction

The Lamb wave, initially introduced by Horace Lamb in 1881 (Lamb, 1881), is a wave mode that propagates along the surface of a medium with almost negligible amplitude in the vertical direction. In the Earth's atmosphere, Lamb waves are generally confined to the troposphere and could be triggered by significant explosive events, including extreme volcanic eruptions, earthquakes, meteoroid impacts, and large artificial explosions (Leonard & Barnes, 1965; Rose et al., 1961; Symons, 1888; Whipple, 1930). The extraordinary eruption of Tonga volcano (20.54°S, 175.38°W) on 15 January 2022, produced exceptional Lamb waves in the troposphere (Wright et al., 2022), offering a unique opportunity to further investigate the impacts of Lamb on the entire Earth system.

The eruption-induced Lamb wave was characterized as a nearly monochromatic pulse propagating at 308–319 m/s with a period of approximately 25 min (Wright et al., 2022). Subsequent studies suggest that the atmospheric Lamb waves have the potential to transfer energy both downward to the ocean and upward to the upper atmosphere (Carvajal et al., 2022; Heki, 2022; Kubota et al., 2022; Li et al., 2023; Lin et al., 2022; Omira et al., 2022; Zhang et al., 2022), surpassing the previous understanding of being limited to a few scale heights above the Earth's surface (Francis, 1973). While their role in generating fast-traveling tsunamis has been established (Carvajal et al., 2022; Kubota et al., 2022; Omira et al., 2022), their effects on the upper atmosphere remain uncertain.

In the upper atmosphere, considerable research has been devoted to exploring the relationship between tropospheric Lamb waves and traveling ionospheric disturbances (TIDs) (e.g., Heki, 2022; Inchin et al., 2023; Li et al., 2024; Lin et al., 2022; Liu, Morton, et al., 2023; Liu, Wang, et al., 2023; Miyoshi & Shinagawa, 2023;

Takahashi et al., 2023; Tang, 2023; Zhang et al., 2022). These efforts have primarily relied on Total Electron Content (TEC) measurements derived from Global Positioning System (GPS) data to estimate the speed and period of eruption-induced TIDs. However, the relative motion between GPS satellites and ground receivers introduces spatiotemporal mixing in TEC measurements (Hu et al., 2017; Huang et al., 2017), complicating the accurate identification of wave speed and time period. The phase speeds of the potentially Lamb-associated TID vary widely, often between 300 and 400 m/s (Heki, 2022; Lin et al., 2022; Zhang et al., 2022). Furthermore, different phase speeds of Lamb waves are obtained from different techniques, implying a more complicated propagation of Lamb wave (if present) in the upper atmosphere (Inchin et al., 2023; Li et al., 2024; Lin et al., 2022; Liu, Morton, et al., 2023; Liu, Wang, et al., 2023; Miyoshi & Shinagawa, 2023; Takahashi et al., 2023; Tang, 2023).

Vadas et al. (2023a, 2023b) argue that TIDs should not be attributed to Lamb waves unless they exhibit definitive propagation characteristics, that is, a phase speed of around 308–319 m/s and a period of approximately 25 min, as observed in the lower atmosphere, rather than merely falling within a similar range. They emphasize the importance of strict consistency in identifying Lamb wave signatures. This distinction is crucial because both simulations and observations have demonstrated that secondary gravity waves can also generate medium-scale TIDs with phase speeds ranging from 200 to 400 m/s and wavelengths spanning 600–2,000 km, which are consistent with many previously reported features (Figueiredo et al., 2023; Vadas et al., 2023a, 2023b). Therefore, clearly distinguishing between Lamb waves and gravity waves, and conclusively confirming the presence of Lamb waves at ionospheric altitudes, remains a challenge.

In this paper, we provide compelling observational evidence for the existence of Lamb waves at ionospheric altitudes, based on accurate measurements of their propagation properties, which facilitates their distinction from gravity waves. This is achieved by using line-of-sight TEC observations from the BeiDou Geostationary Orbit (GEO) satellites, to enhance sensitivity in detecting Lamb waves. The identification of Lamb L0 mode, not only underscores the relevance of Lamb waves in the lower atmosphere and ocean but also highlights their significant impact on the upper atmosphere, making Lamb waves a crucial focal point in energy transmission from epicenters to the entire Earth system.

2. Methodology

2.1. TECs From BeiDou GEO Satellites

Navigation signals from Global Navigation Satellite Systems (GNSS) satellites experience time delays when passing through the ionosphere. These delays also reflect the characteristics of the Earth's ionosphere along the signal's propagation path. TEC data from BeiDou GEO satellites are employed in this study. The BeiDou system comprises several GEO satellites that remain relatively stationary in relation to ground-based observation stations. This stationary position ensures that the navigation signal's propagation path remains nearly fixed within the Earth's rotation reference frame. Consequently, TEC measurements from GEO satellites are considered more reliable compared to non-GEO navigation satellites, minimizing the spatial-temporal ambiguity in determining the ionospheric wave properties arising from the satellite (or the pierce point) moving (Hu et al., 2017; Huang et al., 2017).

Ground-based stations situated in Australia and Indonesia are strategically chosen along a radial propagation path of the Lamb wave. Ionospheric Pierce Points (IPPs) represent the intersection points between navigation signals and the upper boundary of the ionosphere, assumed to be at 400 km. For each station, the IPPs from different BeiDou GEO satellites share similar latitudes, with longitude differences ranging from 1° to 5°. As illustrated later, the Lamb wave triggered by the volcanic eruption exhibits horizontal propagation along the Earth's surface. In the vertical direction, the Lamb wave-front tilts outward originating from the epicenter. Notably, detecting angles nearly parallel to the Lamb wave-front surface are more sensitive to Lamb waves. This approach allows for the extraction of ionospheric Lamb waves, facilitating an in-depth investigation of their characteristics.

2.2. Simulation by the WACCM-X

The Whole Atmosphere Community Climate Model with thermosphere and ionosphere eXtension (WACCM-X) is used in this study with a horizontal resolution of 0.25° and a vertical resolution of 0.1 scale height throughout the middle and upper atmosphere, except for the top three scale heights, which are set to be 0.25 scale height. The

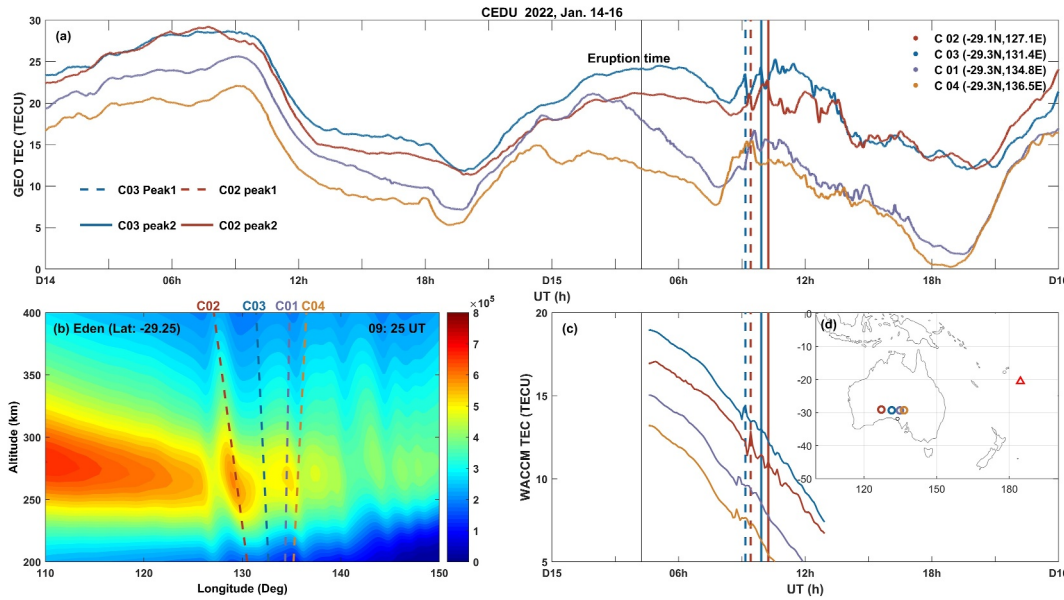

Figure 1. BeiDou TECs from the CEDU station and corresponding Whole Atmosphere Community Climate Model with thermosphere and ionosphere eXtension (WACCM-X) simulations. (a) Total Electron Content (TEC) variations from BeiDou Geostationary Orbit satellites C01–C04 on the eruption day and the day before. The eruption time is denoted by the black vertical line. The blue dashed and solid vertical lines mark the first two TEC peaks observed by C03 at 09:10 UT and 09:55 UT on January 15; the red dashed and solid lines represent similar observations but for C02 at 09:25 UT and 10:15 UT. Offsets of 6, 4, 2, and 0 TECU are added to C03, C02, C01, and C04 for clarity. (b) Simulated electron density (cm^{-3}) from WACCM-X along −29.25° latitude at 09:25 UT when the first peak was detected by C02. Dashed lines show signal paths from BeiDou satellites to CEDU. (c) Simulated TECs from WACCM-X corresponding to the observations in the top panel. (d) Locations of the CEDU station (black circle) and satellite Ionospheric Pierce Points (colored circles). The Tonga volcano is shown as a red triangle.

volcanic eruption is initiated by introducing a surface pressure perturbation of 50 hPa over a radius of 60 km around the epicenter. The initial surface pressure perturbation is obtained through barometric observations, as detailed in Liu, Wang, et al. (2023), and the simulated electron density is employed in the study.

3. Results

Figure 1 provides an example of the variations of BeiDou TECs from the CEDU station (Figure 1a) and corresponding WACCM-X simulations (Figures 1b and 1c) during the 15 January 2022 Tonga eruption. Figure 1a shows TECs from four BeiDou GEO satellites (C01-C04) observed at the CEDU station, located in central Australia, approximately 5,500 km west of the Tonga volcano. TEC observations from all four GEO satellites reveal significant disturbances following the major eruption at 04:15 UT on 15 January, compared to the non-eruption case on January 14. In this paper, the high accuracy of BeiDou GEO measurements allows for a more detailed analysis of the fine structures of the ionospheric disturbances induced by the eruption, emphasizing the distinct behaviors observed across the different satellites.

We categorize the TEC observations into two groups: GEO satellites C03 and C02, with IPPs positioned west of the CEDU station (blue and red circles), and C01 and C04 to the east (purple and yellow circles in Figure 1d). For the TEC observed from C03 (blue curve), two consecutive TEC peaks with substantial amplitudes of ∼3 TECU were observed at 09:10 UT (dashed blue vertical line) and 09:55 UT (solid blue vertical line). TEC variations from the C02 satellite (red curve) exhibit a similar pattern to that from C03 (blue curve), but with a slight phase delay of about 15 min. Following this two-peak pattern are a series of complex and broad-spectrum fluctuations, potentially associated with gravity waves (Vadas et al., 2023a, 2023b). However, the two consecutive peaks were not clearly observed by the C01 (purple curve) and C04 (yellow curve) satellites.

The WACCM-X, which has reproduced Lamb waves (Liu, Wang, et al., 2023), is employed to investigate the Lamb-induced ionospheric disturbances. Figure 1b illustrates the simulated vertical distribution of electron

density along −29.25° latitude, with the four IPPs corresponding to CEDU almost aligned along this latitude, showing the vertical structure of the Lamb waves. At 09:25 UT, along −29.25° latitude, the Lamb waves exhibited tilted wave-fronts with leading phases at higher altitudes. Simultaneously, the signal path from the C02 satellite (red dashed line) tilted westward at an angle of approximately 45° from the vertical direction, aligning with the Lamb wave-front. Along this detection angle, the electron density experienced an enhancement, leading to a significant increase in TEC which is calculated by integrating electron density along the radio path.

The simulated TEC of C02 is plotted in Figure 1c (red solid line), showing a substantial peak of almost 2 TECU at 09:25 UT, consistent with the observation in Figure 1a (red solid line). Similarly, the TEC peak observed by the C03 satellite at 09:10 UT is reproduced by WACCM-X, as indicated by the blue solid lines in Figures 1a and 1c. Since the IPP of C03 is closer to Tonga, the TEC peak of C03 occurred about 15 min earlier than that of C02. It should be noted that WACCM-X setup in this study adopted a highly idealized wave source (a step function perturbation in surface pressure at the eruption site), which may not fully represent the complex atmospheric response to the Tonga eruption. The large-scale ionospheric variations (TEC increase after ∼08 UT), and the broad-spectrum fluctuations following Lamb waves (not shown) could be associated with gravity waves (Vadas et al., 2023a, 2023b). On the other hand, the radio rays from C01 and C04 satellites tilted eastward (shown by dashed purple and yellow lines in Figure 1b). In this scenario, the radio ray directions deviated from being parallel to the Lamb wave-front. When integrating electron density along the ray path to calculate the corresponding TECs, the integral path encompassed both peaks and valleys in electron density. Consequently, the TEC responses associated with Lamb waves experienced significant attenuation, and the simulated TEC responses were less than 0.5 TECU, as shown by the solid purple and yellow lines in Figure 1c.

Figure 2 sketches the propagation of Lamb waves from the Earth's surface to the ionosphere to further interpret the observed phenomenon at CEDU station. The eruption of the Tonga volcano triggered Lamb wave (L0 mode) propagating along the Earth's surface at approximately sound speed, marked by the blue circle in Figure 2. The Lamb wave then induced atmospheric fluctuations at various altitudes. Simulations suggested Lamb waves keep a nearly constant phase speed below ∼120 km as symbolized by the gray circle (e.g., Liu, Wang, et al., 2023; Miyoshi & Shinagawa, 2023; Shinagawa & Miyoshi, 2024; Wu et al., 2023). While in the upper atmosphere, the phase of Lamb wave-associated disturbances at higher altitudes is ahead of that at lower altitudes, creating a three-dimensional conical structure near the epicenter with larger radii at higher altitudes and smaller ones at lower altitudes, as illustrated by the blue and red conical surfaces in Figure 2. An approximately axisymmetric structure is implied by simulations and assimilations based on GNSS TECs (Liu, Wang, et al., 2023; Zhai et al., 2025), although potential directional asymmetries may still exist. Note that the sketched wave-fronts do not represent the actual tilt angle of the Lamb wave-fronts. A complete conical structure requires simultaneous global observations for validation. Since our observations are limited to the Australia and Indonesia region, the presence of global-scale asymmetries possibly influenced by background winds and upper atmospheric dynamics (Liu, Morton et al., 2023) remains uncertain and requires further validation through globally distributed measurements.

Ground stations receive signals from navigation satellites. When the signal path aligns parallel to the Lamb wave-front triggered by the volcanic eruption (the signal path with red dashed line in Figure 2), disturbances in the ionosphere caused by Lamb waves are detected with large wave amplitudes. Conversely, when the path is perpendicular to the wave-front, cancellation effects due to out-of-phase waves along the integration path reduce the measured Lamb wave amplitudes (the signal path with black dashed line in Figure 2).

Due to the relatively short wavelengths of Lamb waves, typically only a few hundred kilometers, distinguishing them in space-based observations is challenging. This has fueled ongoing debate about whether Lamb wave energy can penetrate into the upper atmosphere. However, the fixed geometry of the radio path between a BeiDou GEO satellite and a receiver avoids spatial-temporal ambiguity in detecting Lamb waves which are characterized with medium-scale wavelengths, providing valuable insights into the characteristics of the ionospheric Lamb waves.

This BeiDou GEO-based strategy is employed for observational stations across Australia to investigate the characteristics of ionospheric signatures of Lamb waves. The selection of these stations is predicated on the fact that the propagation direction of the Lamb wave in Australia is approximately along the latitude, as depicted by the horizontal distribution of electron density in Figure 3a. This setup allows some of the detection angles to be

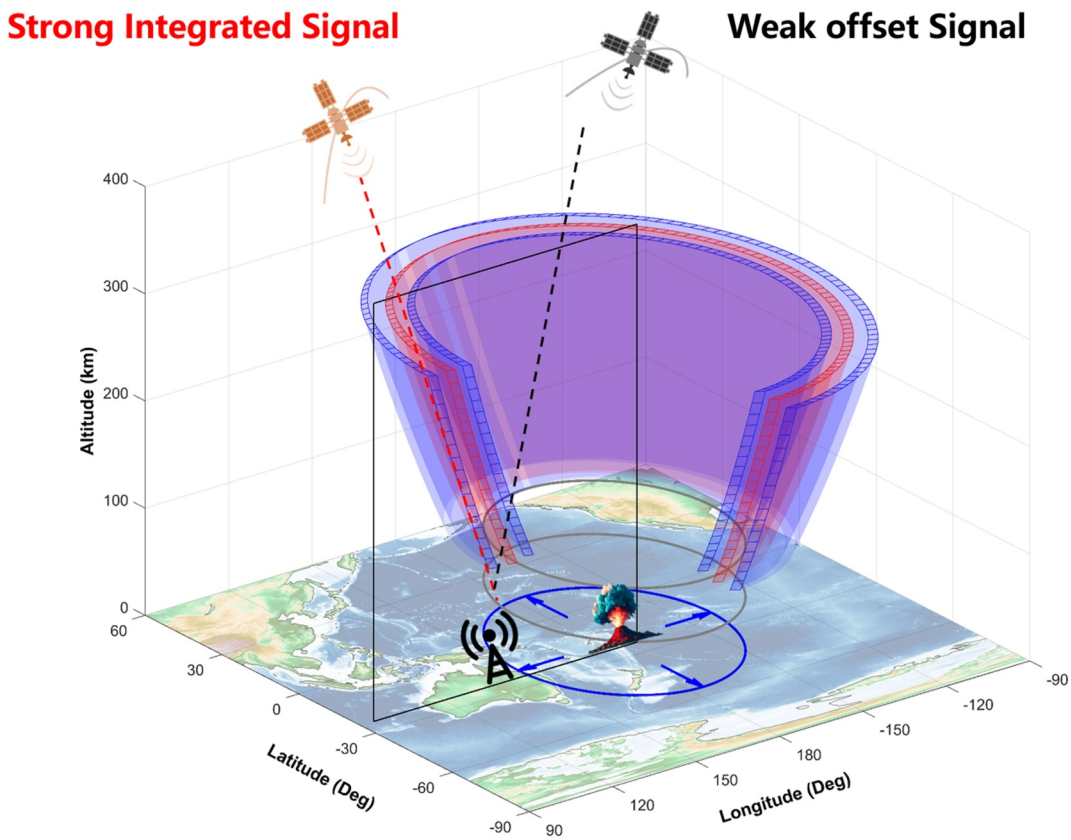

Figure 2. Schematic illustration of spatially propagating Lamb waves triggered by the Tonga eruption. The blue circle represents Lamb waves propagating along the Earth's surface, and the gray curves indicate their upward propagation. Conical surfaces symbolize Lamb waves propagating through the atmosphere, with red and blue indicating wave crests and troughs, respectively. The red line represents the signal path, which is nearly parallel to the wave-front, enhancing the integrated Total Electron Content response, while the black line stands for the nearly perpendicular one, leading to partial cancellation. The black rectangle marks a vertical plane at −29.25° latitude, corresponding to the altitude–latitude section shown in Figure 1b.

oriented parallel to the Lamb wave-front, considering the conical structure of the ionospheric Lamb wave. Specifically, TEC measurements from C02, C03, and C05 satellites, exhibiting greater sensitivity to ionospheric Lamb waves due to their detecting angles tilting outwards from the epicenter, are selected for further analysis. Subsequently, Lamb-involved TEC peaks are manually identified. The times of occurrence of these TEC peaks and the distances between the selected pierce points and the epicenter are linearly fitted, as illustrated in Figure 3a. The propagation speed of the leading TEC peak is determined to be 323.2 ± 10.7 m/s, while the second peak has a speed of 283.5 ± 6.9 m/s. The propagation speed of the observed leading peak is consistent with that of the simulated Lamb L0 mode from WACCM-X (~320 m/s, Liu, Wang, et al., 2023).

The wave periodicity is a crucial property for classifying the observed TEC peaks. By utilizing a 30-min detrend window, we extracted TEC changes relative to the background. The TEC relative changes for all stations are presented in Figure 3b, organized by their distances from the epicenter. From approximately 8 UT to 10 UT, two consecutive peaks with similar amplitudes were identified, propagating from the east coast of Australia (SYDN, etc.) to the west coast (KARR, etc.). These peaks have magnitudes of approximately 1–3 TECU. The distances between the two peaks gradually increased since the leading peaks moved faster. These two consecutive peaks represent TIDs with periods of approximately 30 min. Observations from GOES satellites and global atmospheric pressure records indicate that the time period of the eruption-induced Lamb wave in the troposphere is 25–40 min (Amores et al., 2022; Wright et al., 2022). Therefore, the ionospheric waves we observed following the Tonga eruption share similar time periods with tropospheric Lamb waves.

It should be pointed out that some secondary gravity waves generated by the eruption could also have a similar speed to the Lamb wave, as simulated by Vadas et al. (2023b). However, the time periods of these secondary gravity

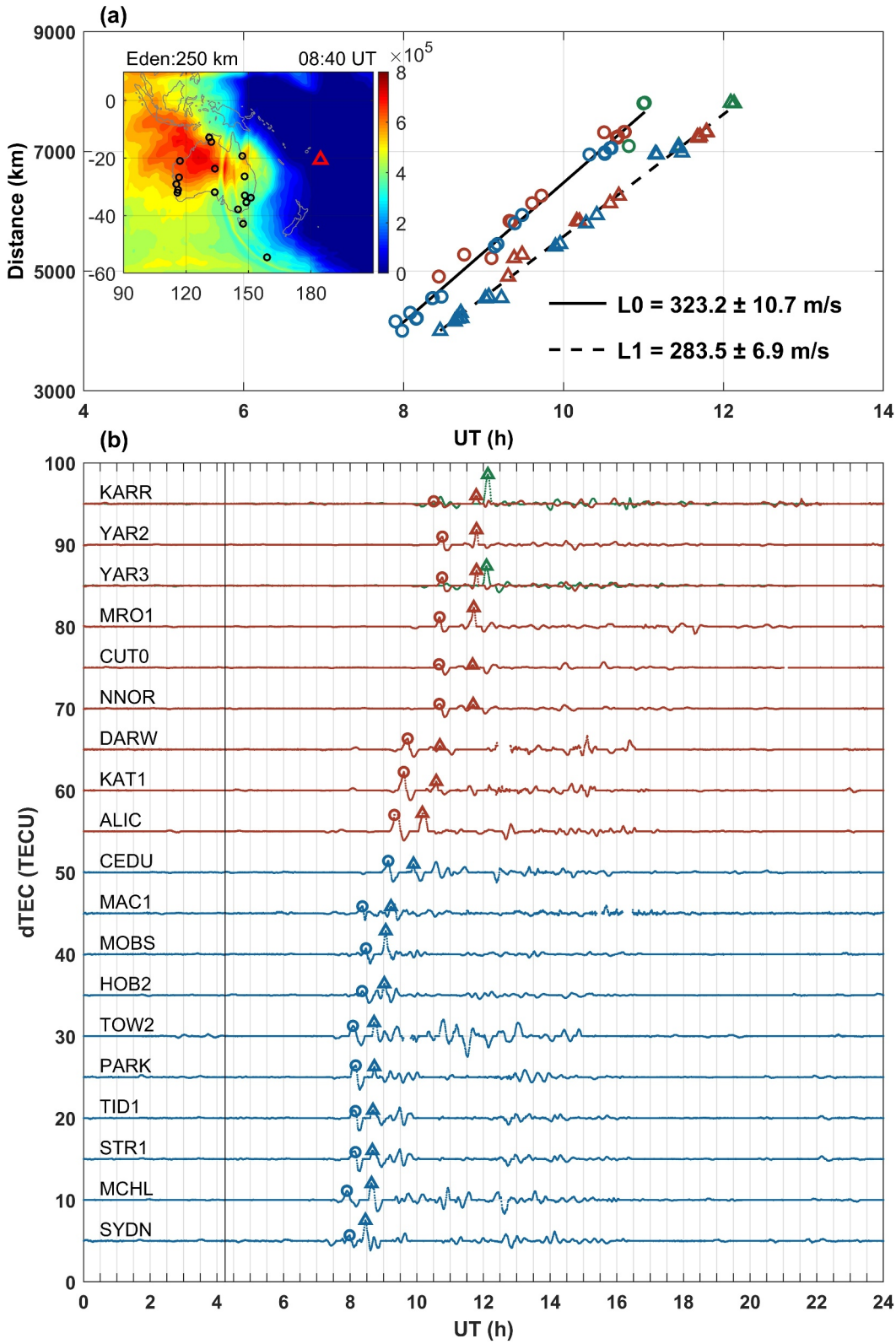

Figure 3. (a) Linear fits of Total Electron Content (TEC) peak times versus distances from Ionospheric Pierce Points of BeiDou satellites (C02: red, C03: blue, C05: green) to the Tonga volcano. Circles and triangles indicate the first and second TEC peaks, respectively. The contour shows the simulated electron density (cm^{-3}) at 08:40 UT. Ground stations and the Tonga volcano are marked by black circles and a red triangle. (b) TEC disturbances from representative GEO satellites after removing 30-min smoothed background. Stations are ordered by increasing distance from the volcano (SYDN to KARR), with an offset of 5 TECU.

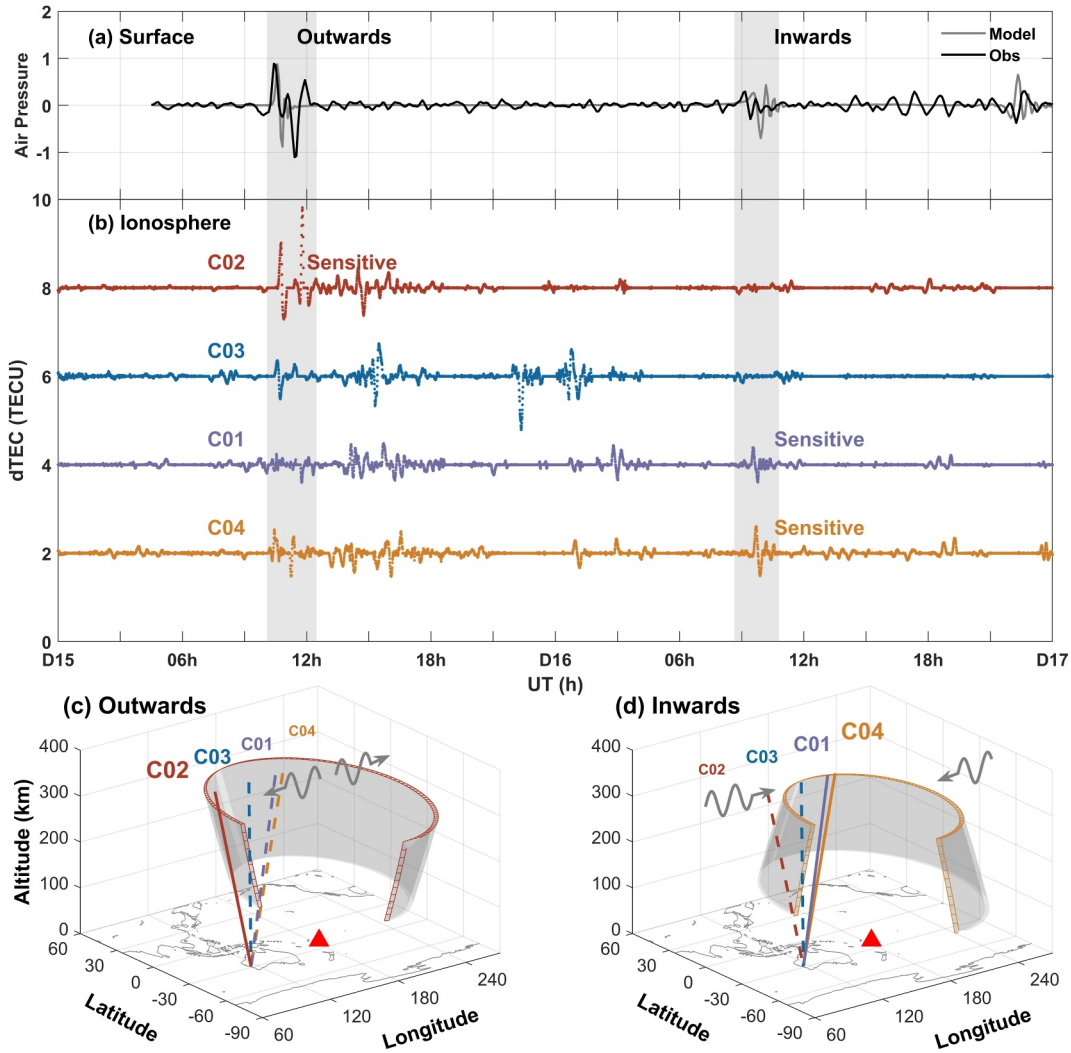

Figure 4. (a) Simulated (gray) and observed (black) surface pressure (hPa) at Perth Airport (Amores et al., 2022). (b) Absolute changes in BeiDou TECs from the YARR station after 30-min smoothing and detrending. Offsets of 8, 6, 4, and 2 TECU are added to C02, C03, C01, and C04, respectively, for clarity. Gray shading marks the Lamb waves passing the YARR station for the first and second times. Schematic illustration of (c) the outward-propagating Lamb wave from Tonga and (d) returning Lamb wave converging to Tonga. In panel (c), C02 (red) is most aligned with the wave-front, showing the strongest response, while in the panel (d) C01 and C04 (purple and yellow) exhibit stronger responses as their signal paths are better aligned with the wave-front.

waves range from 45 to 120 min, which are much larger than our observations. This suggests that the disturbances in TEC with the period of about 30 min we extracted are unlikely related to secondary gravity waves in earlier reports, even though secondary gravity waves are also important sources to the upper atmosphere (Li et al., 2025; Vadas et al., 2023a, 2023b).

The eruption-induced Lamb waves can propagate several times around the Earth in the troposphere (Amores et al., 2022), as recorded by the surface barometer (Figure 4a). Our results in Figure 4 demonstrate that the ionospheric Lamb L0 mode can also circumnavigate the Earth almost entirely. After the Lamb-associated ionospheric disturbances were first detected in Australia, we observed the returning signals after their traveling nearly the entire circumference of the Earth and converging toward Tonga. Figure 4b depicts Lamb waves recorded at the YARR station in the southwestern Australia. Around 10:30 UT on January 15th, the westward-propagating waves arrived. The westward-tilted C02 signal path (red line in Figure 4b) showed more sensitivity in detecting the westward-tilted wave-front (Figure 4c). On the other hand, the direction of C03 is almost vertical, while C01 and C04 are eastward, causing the signal to pass through both wave crests and troughs, and

lead to a reduced Lamb signal. However, the signal propagation path is not strictly perpendicular to the wave-front, and the integration process may not completely cancel out the effects of the crests and troughs. Therefore, the first TEC peak related to the Lamb wave is still visible in C04 observation. Nonetheless, the amplitude of the disturbance in this case is certainly smaller than that observed by C02, where the signal path is nearly parallel to the wave-front.

Around 9 UT on the 16th, the eastward-propagating waves circled nearly the Earth's circumference and were again detected by the YARR station. In contrast to the detected initial disturbances, the returning waves exhibited an eastward-tilted wave-front. This orientation enhances the sensitivity of Lamb wave detection when the GEO satellite pierce point is east of the observation station (with C01 in purple and C04 in yellow), leading to prominent peaks in TEC observations, as indicated by the yellow and purple curves. Similar results from multiple stations could be found in the Supporting Information (Figures S1–S8 in Supporting Information S1). Note that stations on Australia's east coast did not clearly detect signals from the returning ionospheric Lamb waves, likely due to attenuation caused by the continent's complex terrain. Our observations did not clearly or exclusively detect third and subsequent ionospheric Lamb waves. Nevertheless, this persistent nature of TIDs to circle the global atmosphere over a given location is consistent with earlier GNSS results, for example, in the continental U.S. (Zhang et al., 2022), in Japan (Heki, 2022), and in Indonesia (Muafiry et al., 2022), which further supports the relevance of the Lamb wave.

4. Discussion and Summary

The observed ionospheric Lamb waves (Figure 4b) corresponded well with Earth surface Lamb waves detected by pressure records (Figure 4a). The Perth surface pressure measurement station is near the C03 (blue) pierce point, resulting in similar waveform characteristics in both surface pressure and ionospheric TEC observations, initially around 10:30 UT on January 15th and subsequently around 9 UT on the 16th, when Lamb waves initially and subsequently passed near Perth, Australia. The Movie S1 provides a clearer illustration of the correlation between surface-propagating Lamb waves and ionospheric disturbances. Considering that the L0 mode observed in the ionosphere shares a similar speed and time period (wavelength) with that in the troposphere (Wright et al., 2022), the L0 mode in the ionosphere should be continuously driven by the Lamb L0 mode in the troposphere. Although most of the L0 energy is confined to a few scale heights above the Earth's surface, for waves with longer periods than the upper atmospheric Brunt-Väisälä period (~17 min), the L0 would be imperfectly ducted and leak upward into the upper atmosphere (Francis, 1973; Lindzen & Blake, 1972; Nishida et al., 2014; Vadas et al., 2023b; Zhang et al., 2022).

The second TEC peak shows a similar period (~30 min) to the Lamb L0 mode but a slower propagation speed (~284 m/s), as shown in Figure 3. We cautiously suggest that this may be associated with secondary disturbances following the primary Lamb wave (L0 mode). As shown in Figure 1c, the WACCM-X simulation presents a series of secondary fluctuations with similar periods but different speeds after the Lamb L0 mode. The speed of the observed second peak falls within the range of these secondary Lamb-like waves. In fact, some stations also observed a third TEC peak, which may also be related to these secondary Lamb wave disturbances (Figure 1a). Note that the amplitudes of the observed second peak are larger than those in the simulations, possibly due to modulation by gravity waves (Shinagawa & Miyoshi, 2024). Additionally, it is also possible that the multiple eruptions of the volcano (Astafyeva et al., 2022) may contribute to the generation of these subsequent TEC features. Our study focuses on the ionospheric Lamb L0 mode, while the secondary Lamb waves, gravity waves, and their interactions require further investigation in future studies.

In summary, by selecting specific GNSS line-of-sight azimuth and elevation, TEC measurements from BeiDou GEO satellites enable accurate estimation of wave characteristics and the spatial phase front. Our observations show that the ionospheric Lamb wave L0 mode has (a) a phase speed of approximately 323 m/s, (b) a period of around 30 min, and (c) the capacity for global propagation, which are consistent with the characteristics of the tropospheric Lamb wave. Furthermore, the ionospheric Lamb wave manifests as a three-dimensional conical structure radiating outward from the epicenter, with larger radii at higher altitudes and smaller ones at lower altitudes, likely driven by the surface Lamb waves.

Data Availability Statement

BeiDou navigation data are available at Science Data Bank (ScienceDB) via https://doi.org/10.57760/sciencedb.20334 (Li, 2025). WACCM-X simulations are available at Liu, Wang, et al. (2023).

Acknowledgments
This work was supported by the National Natural Science Foundation of China (42188101), the Project of Stable Support for Youth Team in Basic Research Field, CAS (YSBR-018), the B-type Strategic Priority Program of the Chinese Academy of Sciences (XDB0780000), and the International Partnership Program of Chinese Academy of Sciences (Grant 183311KYSB20200003). Ruoxi Li was supported by the National Natural Science Foundation of China (42304171), the China Postdoctoral Science Foundation (2023M733363), the Joint Open Fund of Mengcheng National Geophysical Observatory (MENGO-202314), and the Fundamental Research Funds for the Central Universities (WK2080000220). Work at MIT is supported by US NSF awards AGS-2033787, AGS-2149698, and AGS-1952737, and US NRL Grants N00014-23-1-2160 and N00014-24-1-2122. We acknowledge H.-L Liu for his help in WACCM-X simulation and useful discussions.

References

Amores, A., Monserrat, S., Marcos, M., Argüeso, D., Villalonga, J., Jordà, G., & Gomis, D. (2022). Numerical simulation of atmospheric Lamb waves generated by the 2022 Hunga–Tonga volcanic eruption. *Geophysical Research Letters*, *49*(6), e2022GL098240. https://doi.org/10.1029/2022GL098240

Astafyeva, E., Maletckii, B., Mikesell, T. D., Munaibari, E., Ravanelli, M., Coïsson, P., et al. (2022). The 15 January 2022 Hunga Tonga eruption history as inferred from ionospheric observations. *Geophysical Research Letters*, *49*(10), e2022GL098827. https://doi.org/10.1029/2022GL098827

Carvajal, M., Sepúlveda, I., Gubler, A., & Garreaud, R. (2022). Worldwide signature of the 2022 Tonga volcanic tsunami. *Geophysical Research Letters*, *49*(6), e2022GL098153. https://doi.org/10.1029/2022GL098153

Figueiredo, C. A. O. B., Vadas, S. L., Becker, E., Wrasse, C. M., Takahashi, H., Nyassor, P. K., & Barros, D. (2023). Secondary gravity waves from the Tonga volcano eruption: Observation and modeling over New Zealand and Australia. *Journal of Geophysical Research: Space Physics*, *128*(10), e2023JA031476. https://doi.org/10.1029/2023JA031476

Francis, S. H. (1973). Acoustic-gravity modes and large-scale traveling ionospheric disturbances of a realistic, dissipative atmosphere. *Journal of Geophysical Research*, *78*(13), 2278–2301. https://doi.org/10.1029/ja078i013p02278

Heki, K. (2022). Ionospheric signatures of repeated passages of atmospheric waves by the 2022 Jan. 15 Hunga Tonga–Hunga Ha'apai eruption detected by QZSS-TEC observations in Japan. *Earth Planets and Space*, *74*(1), 1–12. https://doi.org/10.1186/s40623-022-01674-7

Hu, L., Yue, X., & Ning, B. (2017). Development of the Beidou ionospheric observation network in China for space weather monitoring. *Space Weather*, *15*(8), 974–984. https://doi.org/10.1002/2017SW001636

Huang, F., Lei, J., & Dou, X. (2017). Daytime ionospheric longitudinal gradients seen in the observations from a regional BeiDou GEO receiver network. *Journal of Geophysical Research: Space Physics*, *122*(6), 6552–6561. https://doi.org/10.1002/2017JA023881

Inchin, P. A., Bhatt, A., Cummer, S. A., Eckermann, S. D., Harding, B. J., Kuhl, D. D., et al. (2023). Multi-Layer evolution of acoustic-gravity waves and ionospheric disturbances over the United States after the 2022 Hunga Tonga volcano eruption. *AGU Advances*, *4*(6), e2023AV000870. https://doi.org/10.1029/2023AV000870

Kubota, T., Saito, T., & Nishida, K. (2022). Global fast-traveling tsunamis driven by atmospheric Lamb waves on the 2022 Tonga eruption. *Science*, *377*(6601), 91–94. https://doi.org/10.1126/science.abo436

Lamb, H. (1881). On the vibrations of an elastic sphere. *Proceedings of the London Mathematical Society*, *1*(1), 189–212. https://doi.org/10.1112/plms/s1-13.1.189

Leonard, R. S., & Barnes, R. A., Jr. (1965). Observation of ionospheric disturbances following the Alaska earthquake. *Journal of Geophysical Research*, *70*(5), 1250–1253. https://doi.org/10.1029/JZ070i005p01250

Li, R. (2025). Data based on the study of 'ionospheric Lamb waves with conical phase fronts following the 2022 Tonga eruption unveiled by Beidou GEO observations' [Dataset]. *Science Data Bank*. https://doi.org/10.57760/sciencedb.20334

Li, R., Lei, J., Zhang, S.-R., Liu, F., Dang, T., Chen, X., & Meng, X. (2025). Were gravity waves or Lamb waves responsible for the large-scale thermospheric response to the Tonga eruption? *AGU Advances*, *6*(2), e2024AV001470. https://doi.org/10.1029/2024AV001470

Li, X., Ding, F., Xiong, B., Chen, G., Mao, T., Song, Q., & Yu, C. (2024). Multi-wave structures of traveling ionospheric disturbances associated with the 2022 Tonga volcanic eruptions in the New Zealand and Australia regions. *Remote Sensing*, *16*(14), 2668. https://doi.org/10.3390/rs16142668

Li, X., Ding, F., Yue, X., Mao, T., Xiong, B., & Song, Q. (2023). Multiwave structure of traveling ionospheric disturbances excited by the Tonga volcanic eruptions observed by a dense GNSS network in China. *Space Weather*, *21*(2), e2022SW003210. https://doi.org/10.1029/2022SW003210

Lin, J. T., Rajesh, P. K., Lin, C. C., Chou, M. Y., Liu, J. Y., Yue, J., et al. (2022). Rapid conjugate appearance of the giant ionospheric Lamb wave signatures in the northern hemisphere after Hunga-Tonga volcano eruptions. *Geophysical Research Letters*, *49*(8), e2022GL098222. https://doi.org/10.1029/2022GL098222

Lindzen, R. S., & Blake, D. (1972). Lamb waves in the presence of realistic distributions of temperature and dissipation. *Journal of Geophysical Research*, *77*(12), 2166–2176. https://doi.org/10.1029/JC077i012p02166

Liu, H. L., Wang, W., Huba, J. D., Lauritzen, P. H., & Vitt, F. (2023). Atmospheric and ionospheric responses to Hunga–Tonga volcano eruption simulated by WACCM-X. *Geophysical Research Letters*, *50*(10), e2023GL103682. https://doi.org/10.1029/2023GL103682

Liu, L., Morton, Y. J., Cheng, P. H., Amores, A., Wright, C. J., & Hoffmann, L. (2023). Concentric traveling ionospheric disturbances (CTIDs) triggered by the 2022 Tonga volcanic eruption. *Journal of Geophysical Research: Space Physics*, *128*(2), e2022JA030656. https://doi.org/10.1029/2022JA030656

Miyoshi, Y., & Shinagawa, H. (2023). Upward propagation of gravity waves and ionospheric perturbations triggered by the 2022 Hunga–Tonga volcanic eruption. *Earth Planets and Space*, *75*(1), 68. https://doi.org/10.1186/s40623-023-01827-2

Muafiry, I. N., Meilano, I., Heki, K., Wijaya, D. D., & Nugraha, K. A. (2022). Ionospheric disturbances after the 2022 Hunga Tonga–Hunga Ha'apai eruption above Indonesia from GNSS-TEC observations. *Atmosphere*, *13*(10), 1615. https://doi.org/10.3390/atmos13101615

Nishida, K., Kobayashi, N., & Fukao, Y. (2014). Background Lamb waves in the Earth's atmosphere. *Geophysical Journal International*, *196*(1), 312–316. https://doi.org/10.1093/gji/ggt413

Omira, R., Ramalho, R. S., Kim, J., González, P. J., Kadri, U., Miranda, J. M., et al. (2022). Global Tonga tsunami explained by a fast-moving atmospheric source. *Nature*, *609*(7928), 734–740. https://doi.org/10.1038/s41586-022-04926-4

Rose, G., Oksman, J., & Kataja, E. (1961). Round-the-World sound waves produced by the nuclear explosion on October 30, 1961, and their effect on the ionosphere at Sodankylä. *Nature*, *192*(4808), 1173–1174. https://doi.org/10.1038/1921173a0

Shinagawa, H., & Miyoshi, Y. (2024). Simulation study of atmosphere-ionosphere variations driven by the eruption of Hunga Tonga–Hunga Ha'apai on 15 January 2022. *Earth Planets and Space*, *76*(1), 15. https://doi.org/10.1186/s40623-024-01960-6

Symons, G. J. (Ed.) (1888)., *The eruption of Krakatoa and subsequent phenomena.* Report of the Krakatoa Committee of the Royal Society.

Takahashi, H., Figueiredo, C. A. O. B., Barros, D., Wrasse, C. M., Giongo, G. A., Honda, R. H., et al. (2023). Ionospheric disturbances over South America related to Tonga volcanic eruption. *Earth, Planets and Space*, *75*(1), 92. https://doi.org/10.1186/s40623-023-01844-1

Tang, L. (2023). Ionospheric disturbances of the January 15, 2022, Tonga volcanic eruption observed using the GNSS network in New Zealand. *GPS Solutions*, *27*(1), 53. https://doi.org/10.1007/s10291-023-01395-8

Vadas, S. L., Becker, E., Figueiredo, C., Bossert, K., Harding, B. J., & Gasque, L. C. (2023). Primary and secondary gravity waves and large-scale wind changes generated by the Tonga volcanic eruption on 15 January 2022: Modeling and comparison with ICON-MIGHTI winds. *Journal of Geophysical Research: Space Physics*, *128*(2), e2022JA031138. https://doi.org/10.1029/2022JA031138

Vadas, S. L., Figueiredo, C., Becker, E., Huba, J. D., Themens, D. R., Hindley, N. P., et al. (2023). Traveling ionospheric disturbances induced by the secondary gravity waves from the Tonga eruption on 15 January 2022: Modeling with MESORAC/HIAMCM/SAMI3 and comparison with GPS/TEC and ionosonde data. *Journal of Geophysical Research: Space Physics*, *128*(6), e2023JA031408. https://doi.org/10.1029/2023JA031408

Whipple, F. J. W. (1930). The great Siberian meteor and the waves, seismic and aerial, which it produced. *Quarterly Journal of the Royal Meteorological Society*, *56*, 278–304.

Wright, C. J., Hindley, N. P., Alexander, M. J., Barlow, M., Hoffmann, L., Mitchell, C. N., et al. (2022). Surface-to-space atmospheric waves from Hunga Tonga–Hunga Ha'apai eruption. *Nature*, *609*(7928), 741–746. https://doi.org/10.1038/s41586-022-05012-5

Wu, H., Lu, X., Wang, W., & Liu, H. L. (2023). Simulation of the propagation and effects of gravity waves generated by Tonga volcano eruption in the thermosphere and ionosphere using nested-grid TIEGCM. *Journal of Geophysical Research: Space Physics*, *128*(4), e2023JA031354. https://doi.org/10.1029/2023JA031354

Zhai, C., Zhang, S. R., Yao, Y., Dong, W., Aa, E., Kong, J., et al. (2025). Three-dimensional characterization of global ionospheric disturbances during the 15 January 2022 Tonga volcanic eruption. *Geophysical Research Letters*, *52*(2), e2024GL113129. https://doi.org/10.1029/2024GL113129

Zhang, S. R., Vierinen, J., Aa, E., Goncharenko, L. P., Erickson, P. J., Rideout, W., et al. (2022). 2022 Tonga volcanic eruption induced global propagation of ionospheric disturbances via Lamb waves. *Frontiers in Astronomy and Space Sciences*, *9*, 871275. https://doi.org/10.3389/fspas.2022.871275